THE JOURNAL OF PHYSICAL CHEMISTRY C

Article

pubs.acs.org/JPCC

Contact Angle, Liquid Film, and Liquid–Liquid and Liquid–Solid Interfaces in Model Oil–Brine–Substrate Systems

Felipe Jiménez-Ángeles[†] and Abbas Firoozabadi[*,†,‡]

[†]Reservoir Engineering Research Institute, Palo Alto, California 94301, United States

[‡]Department of Chemical and Environmental Engineering, Yale University, New Haven, Connecticut 06510, United States

Supporting Information

ABSTRACT: Oil–water–substrate wettability is of prime importance in most branches of science and technology, from biology and nanomaterials to geology and petroleum science. Wetting is a three-phase interaction phenomenon as expressed in Young's equation. Microscopically wetting is from the fluid–substrate interactions and surfaces are designated as lyophilic and lyophobic (fluid-wet and nonwet). Here we investigate the microscopic mechanisms of wettability changes by salt concentration in oil–water–mineral substrate systems. A model oil droplet (*n*-decane) placed in an aqueous electrolytic solution next to a solid substrate surface (muscovite mica) is simulated. A thin water layer between oil and the substrate regulates the oil–substrate interaction. We find that at zero and low salt concentrations, the oil adsorption on the hydrophilic mineral substrate is stabilized by a thin layer of water giving rise to a nonzero contact angle (partial oil wetting). As the salt concentration increases ionic adsorption and the water layer thickness increase reducing the oil–substrate wettability. Ions adsorb unsymmetrically on the substrate and promote water adsorption into the water layer. Ionic adsorption is higher away from the droplet than under the droplet. Our contact angles by molecular dynamics simulations are in agreement with experimental measurements.

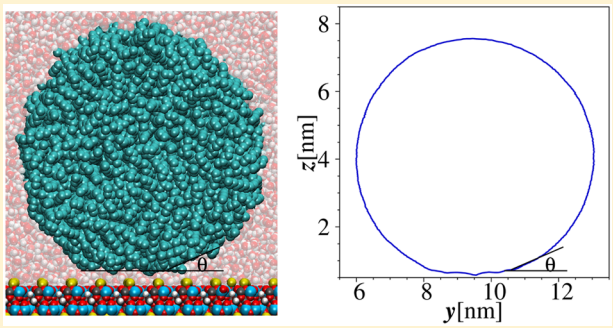

INTRODUCTION

Wettability is the property of a fluid to spread on a substrate in the presence of another fluid. Wetting is the result of the interplay of molecular interactions among three phases and is quantified by the contact angle.[1,2] The mechanisms governing wettability are the subject of current interest in fundamental and applied research. Fluid–substrate wettability and oil–water interface have a profound technological importance due to different types of oil used in food, fuel, lubrication, paints, plastics, cosmetics, and other materials. Ions can form when there is water; the oil–brine–substrate system is found in living organisms, industrial processes, and geological formations.[3,4] Tunning of oil–water–substrate wettability in nanomaterials is used for environmental stewardships.[5−7]

Water injection into geological reservoirs is employed for hydrocarbon production.[8] Low-salinity water injection may improve oil recovery due to changes in the oil–water-rock wettability.[9,10] Recent laboratory measurements indicate that ion adsorption induces wetting transitions in model oil–water–mineral substrate systems.[11] Similar measurements performed using crude oils show that the contact angle has a non-monotonic trend as a function of the salt concentration;[12] in the low salinity regime the oil–substrate wettability is minimum. A water layer between oil and rock and variations of the thickness with salt concentration and ions type have been measured.[13,14] The mechanisms of wettability alteration in oil–brine–mineral substrate systems have not been clarified.

Molecular dynamics simulations have been used to study contact angle in vapor–liquid–solid substrate systems. The vapor–liquid interface of Lennard-Jones model fluids[15−19] and the vapor–liquid interface of water cover most of the reports in the literature. Other investigations of vapor–liquid systems include linear chains,[20,21] and ethanol[22,23] and surfactant aqueous solutions.[24−26] The solid substrates studied include carbon material such as nanotubes, graphite, and graphene,[27−33] metals and minerals,[34−39] polymers[40,41] and complex heterogeneous materials.[42,43] Gas–liquid–solid[44,45] contact angle has been simulated using CO_2 (gas), ionic aqueous solutions (liquid), and quartz and gibbsite as subtrates (solid). The liquid–liquid–solid substrate contact angle has important computational challenges and has been rarely studied.[46,47]

In this investigation we simulate liquid–liquid–solid contact angle of a model oil, an ionic aqueous solution, and the mica mineral substrate; the model oil is *n*-decane. Our simulations elucidate molecular mechanisms in the changes of wettability from salt concentration; the results are in agreement with measurements.

Received: February 13, 2016
Revised: April 15, 2016
Published: May 10, 2016

ACS Publications © 2016 American Chemical Society

DOI: 10.1021/acs.jpcc.6b01521
J. Phys. Chem. C 2016, 120, 11910−11917

■ MODEL AND SIMULATION METHOD

We simulate an oil droplet-aqueous solution-mica substrate system; the salt concentration in the aqueous solution is represented by ρ_s. The simulated setup and the molecular representation of the components are shown in Figure 1, parts a and b, respectively. Cylindrical geometry of the droplet is used[18,45] to remove the line tension effects and to represent macroscopic oil−water−substrate contact.[8] The model oil droplet is composed of 2340 *n*-decane ($C_{10}H_{22}$) linear chains which are simulated using the united atom model potentials for alkanes;[48] CH_n (n = 2,3) groups are uncharged spherical particles joined by bond constraints; bending and torsion potentials are imposed in triplets and quadruplets of consecutive atoms, respectively. Water molecules are represented by the simple charge model,[49] and Na^+ and Cl^- ions as charged spherical particles using the OPLS force field.[50] The composition of the aqueous solutions is given in Table 1.

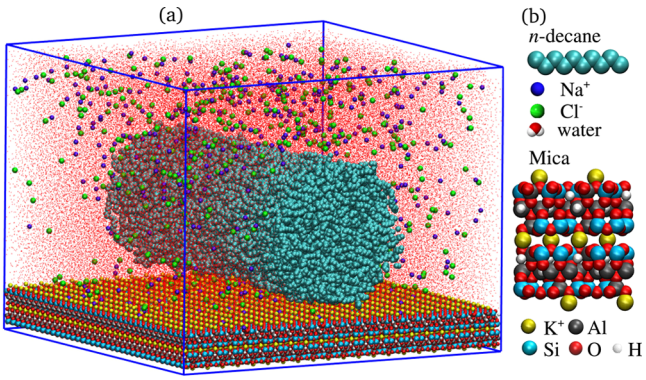

Figure 1. (a) Rotated view of the simulated setup showing water in the bulk solution as red points. (b) Molecular representations: *n*-decane ($C_{10}H_{22}$) is a chain of 10 CH_n-beads (cyan); Na^+ and Cl^- ions are spherical particles colored in blue and green, respectively; water is a three-site molecule with oxygen represented in red and hydrogen in white. The components of muscovite mica ($K_2Al_4(Al_2Si_6)O_{20}(OH)_4$) are colored according to the code: Si, light blue; Al, gray; K, yellow; O, red; H, white.

Table 1. Simulation Setups[a]

run	N_w	N_d	$N^+ = N^-$	ρ_s [wt %]
1	111133	2340	0	0
2	114547	2340	53	0.15
3	114450	2340	393	1.1
4	114381	2340	1232	3.4
5	125045	2340	3215	7.7

[a] N_w = number of water molecules, N_d = number of *n*-decane molecules, and N^+ and N^- = number of sodium and chlorine ions, respectively; ρ_s is the salt concentration in weight %.

The muscovite mica substrate ($K_2Al_4(Al_2Si_6)O_{20}(OH)_4$) is represented by the atomic coordinates and partial charges.[51,52] The mica surface charge density of −0.3424 C/m^2 (equivalent to −2.14 e/nm^2; e is the elementary charge) is neutralized by the K^+ ions from the substrate outermost layer (2.14 K^+ ions/nm^2). The substrate dimensions are 18.7 nm ×18.9 nm ×2 nm in the x, y, and z directions, respectively (36 × 21 × 1 unit cells). The structure of muscovite is shown in Figure 1b. The substrate atoms other than the outermost layer of potassium are kept fixed applying position restraints. The positions of most K^+ ions remain nearly unaltered during the pre-equilibration and equilibration simulations. Depending on ρ_s some K^+ ions may dissolve into the aqueous phase. We will come back to this point later when we discuss the ionic adsorption.

To allow for the hydration of the substrate, pre-equilibration of the surface is carried out by placing it next to an aqueous solution having a salt concentration ρ_s and equilibrated by means of a 3 ns molecular dynamics simulation. Additional 10 ns are used to obtain the density profiles. The ions and water molecules above a distance z_h from the substrate are removed and molecules within $z < z_h$ are kept as part of the hydrated substrate; z is measured from the outermost layer of oxygen atoms from the substrate. The value of z_h is established based on the perpendicular density profiles; it varies from z_h = 0.8 nm at 0 wt % NaCl to z_h = 1.0 nm at 7.7 wt % NaCl. Details of the pre-equilibration simulations and the thickness of the water layer are provided in Table S1. Snapshots of the pre-equilibration substrate−solution setup and the water layer adsorbed onto the substrate are shown in panels a and b of Figure S1, respectively (see Supporting Information).

The droplet is built by placing the 2340 *n*-decane molecules in a prismatic box of approximately 18 nm ×6.5 nm ×7.0 nm forming five layers, each layer is made of 468 molecules. Aqueous solutions are prepared separately in three prismatic boxes, two of them of 18.6 nm × 6.1 nm × 7 nm and a third one of 18.5 nm ×18.7 nm ×5 nm, respectively (see panel a in Figure S1 in the Supporting Information). A 2 ns MD simulation is performed under 3D periodic boundary conditions at T = 298 K and P_z = 200 bar. The pressure is controlled using an anisotropic Berendsen thermostat with relaxation time τ_P = 0.2 ns. To adjust the pressure the box is allowed to fluctuate along the z direction. The system evolves toward a cylindrical droplet (see panel b in Figure S1 in the Supporting Information). The cylindrical droplet in an aqueous electrolytic solution at salt concentration ρ_s and the pre-equilibrated substrate are assembled in the simulations setup shown in Figure 1a; the droplet is placed on top of the water layer from the pre-equilibration step. The composition details of the simulated setups are given in Table 1.

Periodic boundary conditions are applied in the x and y directions. In the z-direction the simulation box is constrained by a virtual wall at $z = l_z$ by means of a 9−3 Lennard-Jones potential given by[53] $u_{ij}^w(z) = 4\epsilon_w\pi\rho_w\sigma_w^3/3[(\sigma_w/z)^9/15 - (\sigma_w/z)^3/2]$; z is the perpendicular distance to the wall, ρ_w = 20 atoms/nm^3, ϵ_w = 1.13 kJ/mol, and σ_w = 0.37 nm. The attractive effect of the wall vanishes at a distance of about 1 nm. In all our simulations there is a separation distance of about 4.5 nm between the wall at the top and the droplet; the top wall does not affect our results. The simulation box has dimensions of l_x = 18.7 nm and l_y = 18.9 nm in the x and y directions, respectively. Newton's equation of motion is integrated using the leapfrog algorithm. Intermolecular interactions are taken into account through the Lennard-Jones and Coulomb potentials. The Lennard-Jones interactions are truncated at 1.2 nm and long-range electrostatic interactions are computed using the smooth particle mesh Ewald summation in slab geometry.[54] A vacuum space of $3l_z$ between image boxes along the z direction warrants a negligible effect of periodic boundary conditions.[54] Berendsen thermostat (τ_T = 0.2 ns) and barostat (τ_P = 0.2 ns) are used to stabilize temperature and pressure at T = 298 K and P_z = 200 bar during the initial 200 ps of simulations. A long simulation run in the NVT ensemble at T = 298 K using the Nosé−Hoover[55,56] thermostat with a relaxation time of τ_T = 2 ps is

DOI: 10.1021/acs.jpcc.6b01521
J. Phys. Chem. C 2016, 120, 11910−11917

used for the equilibration and production; the pressure stays at about $P_z \sim 200$ bar. This pressure can be found at geological conditions in oil reservoirs. Pressure has a minor effect because the two immiscible liquid phases are nearly incompressible. Simulations are conducted using the open source code Gromacs.[57,58]

The density profile of n-decane CH_n beads in the $y-z$ plane $\rho_d(y,z)$ is computed using a grid of 200 × 200 nodes and averaging over configurations sampled at intervals of 1 ps. The droplet shape is outlined by a contour plot defined by $\rho_d(y,z) = 0.5\ \rho_b$, where $\rho_b = 55$ mol/L is the average bulk density of n-decane beads at the center of the droplet. The equilibrium criterion is established when no significant differences are detected between two profiles obtained from two consecutive intervals of 1.5 ns. This condition is reached after 20 ns of simulation. The reported profiles are obtained by taking average over the last 3 ns of simulation.

Contact Angle Calculation Method. In the interfacial region, density contour profiles ($\rho_d(y,z)$ = constant) are circular and concentric. The profiles can be fitted by a circle given by $(y - y_0)^2 + (z - z_0)^2 = R^2$; y_0 and z_0 are the circle center coordinates and R is the circle radius. Figures 2 shows the density contour profile at the surface at $\rho_d(y,z) = 0.5\rho_b$ from run 1 at 0 NaCl wt % and the fitted circle. The contact angle θ is formed by (1) the vertical line passing through the circle's center and (2) the line connecting the circle's center and the intersection point of the droplet profile and the horizontal contact plane at (y_c,z_c) (see Figure 2). The contact plane is defined where the droplet profile deviates from circular shape toward a rough interface using the criterion $\alpha = |r_c - R|/R > 0.03$, where $r_c = \sqrt{(y_c - x_0)^2 + (z_c - z_0)^2}$. The deviation can be examined visually at the bottom of the profiles (see Figure 2). The contact angle is obtained from $\tan\theta = (y_c - y_0)/(z_c - z_0)$. The interface thickness defined between $\rho_d(y,z) = 0.8\rho_b$ and $0.2\rho_b$ is about 0.4 nm. By computing the contact angle within the interval $(0.2\rho_b, 0.8\rho_b)$ the contact angle variation is less than 0.5°. This value is taken as the accuracy of our contact angle. Our contact angle calculation method gives similar results as the methods in refs.[16,18] The density contour plots used to determine the contact angle from our molecular dynamics simulations from 0.15 to 7.7 NaCl wt % are provided in Figures S2−S5.

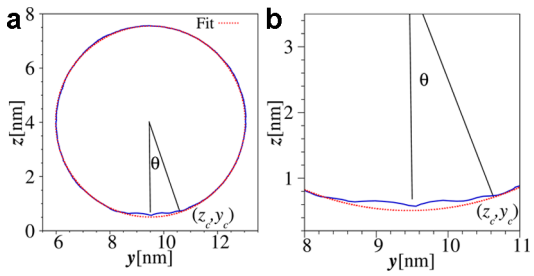

Figure 2. (a) Droplet shape at ρ_s = 0 wt % NaCl defined by the number density contour plot of carbon atoms of n-decane at $\rho_d(y,z) = 0.5\rho_b$. The contact angle θ is obtained from a fitted circle (red-dashed line) and its intersection at z_c = 0.72 nm. (b) Closeup view of the profile where the contact angle is defined.

RESULTS

Our study is centered on the droplet shape and contact angle, the thickness and structure of the fluid confined between the droplet and the substrate, and the fluid structure outside the droplet. We also present simulation results of the fluid structure close to the substrate in the pre-equilibration before introducing the droplet.

Parts a and b of Figure 3 show instantaneous snapshots of the cylindrical droplet equilibrated by more than 20 ns of molecular dynamics simulations (top) and the average density contour profile of n-decane at $\rho_d(y,z) \approx 0.5\rho_b$ (bottom). The density contour plots are circular at the upper part and nearly flat at the bottom. At 0 NaCl concentration (Figure 3a) the contact angle in the aqueous phase from our molecular dynamics simulation is θ = 18.8° which in agreement with the reported experimental value of θ = 17°.[59] At 3.4 NaCl wt % (Figure 3b) the flat section of the droplet is narrower than at 0

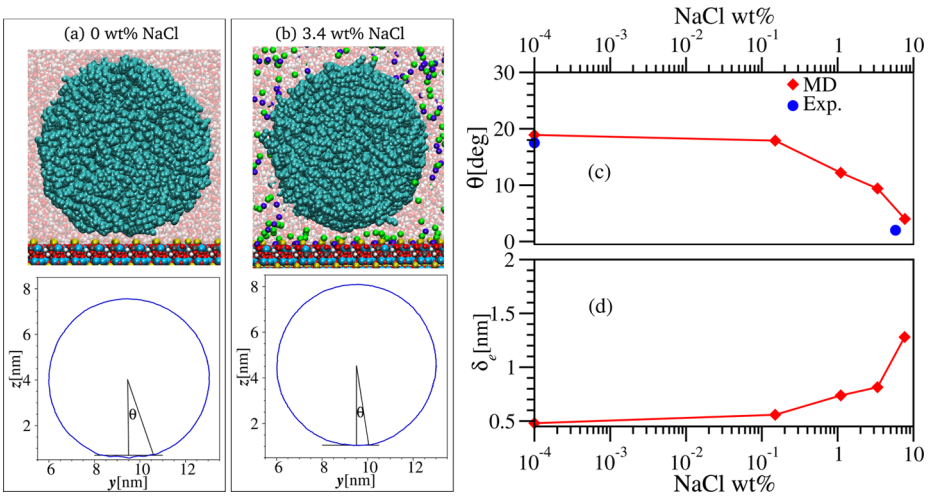

Figure 3. Decane droplet in aqueous solutions at (a) ρ_s = 0 and (b) ρ_s = 3.4 wt % NaCl; instantaneous snapshot of the droplet equilibrated by molecular dynamics simulations (top) and time averaged contour profile at $\rho_d(y,z) = 0.5\ \rho_b$ (bottom). (c) Contact angle θ in the aqueous phase as a function of salt concentration; the results from MD simulations are represented as filled diamonds whereas the straight lines joining them are used to guide the view. The experimental measurements (filled circles) are reported at 0 and 5.8 NaCl wt % in refs 59 and 11, respectively. (d) Water layer thickness as a function of salt concentration from molecular dynamics simulations.

DOI: 10.1021/acs.jpcc.6b01521
J. Phys. Chem. C 2016, 120, 11910−11917

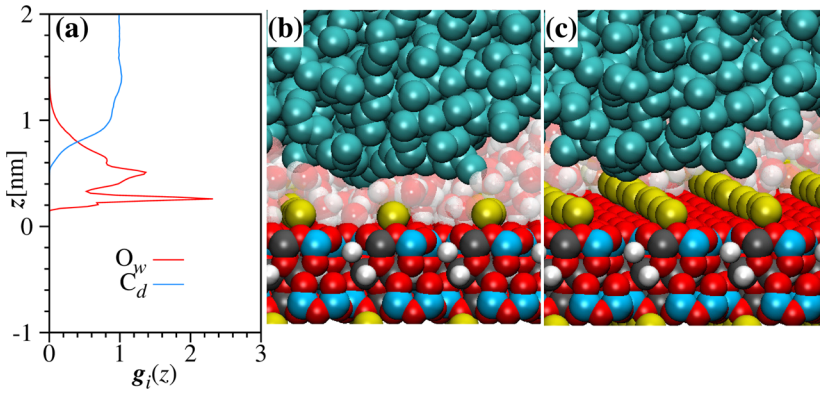

Figure 4. Liquid layer between the droplet and the substrate at 0 wt % NaCl: (a) Reduced density profiles of water oxygen atoms O_w and *n*-decane carbon atoms C_d. (b and c) Front and rotated views, respectively, of the liquid layer region between the droplet and the substrate. The origin of the perpendicular distance to the substrate is placed above the outermost layer of oxygen atoms from the substrate. The scales along the *z* direction in parts a and b match. Water molecules are shown in the background semitransparently, and the color code is the same as in Figure 1.

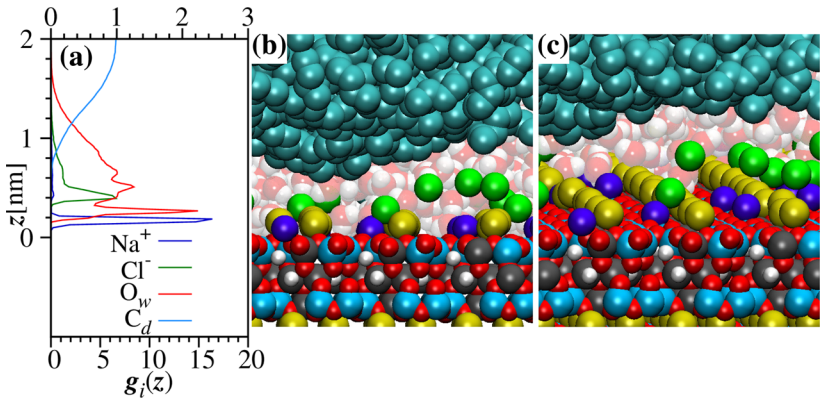

Figure 5. Liquid layer between the droplet and the substrate at 3.4 wt % NaCl: (a) Reduced density profiles of Na^+ and Cl^- ions, water oxygen O_w, and *n*-decane carbon atoms C_d; the scale at the top is for water and *n*-decane, the scale at the bottom is for the ions. The density profiles are computed within a 3 nm strip along the *y* direction. (b and c) Front and rotated views, respectively, of the liquid layer region between the droplet and the substrate. The origin of the perpendicular distance to the substrate is placed above the outermost layer of oxygen atoms from the substrate. The scales along the *z* direction in parts a and b match. Water molecules are shown in the background semitransparently and the color code is the same as in Figure 1.

NaCl wt % and the contact angle is 7°. At the beginning of the simulation the droplet is separated from the substrate by the water layer from pre-equilibration. The equilibrium separation distance between the droplet and the substrate is established during the equilibration process; the droplet approaches or separates from the surface by diffusion. We note that at 3.4 NaCl wt % the density contour profile is farther from the substrate than at 0 NaCl wt % implying an increase of thickness of the water layer between the droplet and the substrate as the salt concentration increases. The contact angle as a function of salt concentration from MD simulations is depicted in Figure 3c. There is no a significant change from 0 to 0.1 NaCl wt % but a monotonic decrease of the contact angle from $\theta = 17.8°$ to 3.5° is observed from 0.1 to 7.7 NaCl wt %. Our simulation results are in agreement with the experimental measurements reported in the literature at 0[59] and 5.8[11] NaCl wt %. The thickness of the liquid layer between the substrate and the droplet δ_e is defined at the *n*-decane-water interface where the water density is one-half of the bulk density. A monotonic increase of the water layer thickness as a function of the salt concentration is portrayed in Figure 3d from $\delta_e = 0.48$ nm at 0 NaCl wt % to $\delta_e \approx 1.3$ nm at 7.7 NaCl wt %. In the following, we discuss the relationship between the contact angle, salt concentration, and water layer thickness.

The liquid layer between the droplet and the substrate at 0 wt % NaCl is shown in Figure 4. The reduced density profiles of water oxygen atoms and carbon atoms from *n*-decane as a function of the perpendicular distance to the substrate are depicted in Figure 4a. The snapshots showing the confinement region are shown in Figure 4, parts b and c. The density profiles are computed within a strip of 3 nm along the *y* direction within the region of closest approach between the droplet and the substrate. The density profiles are normalized with respect to the bulk densities of 53.5 and 55 mol/L for water and *n*-decane, respectively. The density profile of water (see Figure 4a) shows a sharp peak at $z \approx 0.26$ nm and a small hump at $z \approx 0.20$ nm, indicating the location of the water layers adsorbed on the substrate. In the sharp peak the water density is about 2.5 times the water bulk density. A secondary peak is seen close to the oil phase at $z \approx 0.5$ nm and a hump at $z \approx 0.62$ nm. The height of the secondary peak is about 1.3. The position and height of the two peaks are about the same as those from the region outside the droplet (see Figure S8). The water density profile drops monotonically to zero toward the oil droplet. The water layer thickness is measured from the sharp peak at $z \approx$

DOI: 10.1021/acs.jpcc.6b01521
J. Phys. Chem. C 2016, 120, 11910−11917

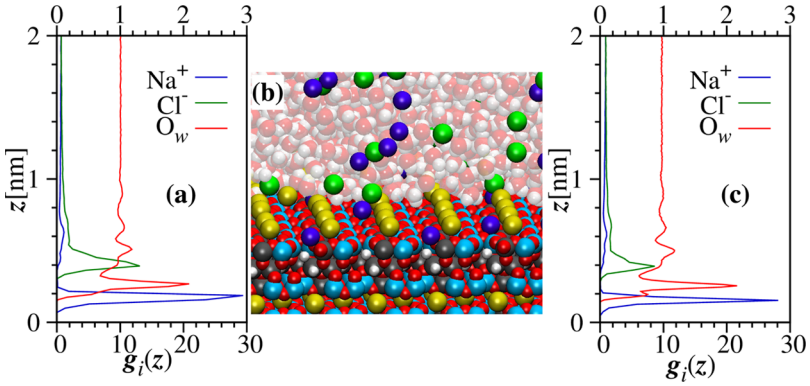

Figure 6. Liquid−solid interface at 3.4 wt % NaCl. (a) Reduced density profiles away from the droplet; ions Na^+ and Cl^-, and water oxygen atoms O_w. (b) Snapshot showing the ions, water, and *n*-decane molecules in the liquid−solid interface. Water molecules are shown in the background semitransparently and the color code is the same as in Figure 1. (c) Reduced density profiles from the substrate pre-equilibration. The scale at the top is for water and *n*-decane; the scale at the bottom is for the ions.

0.26 nm to the point where the reduced density profile is 0.5. The reduced density profile of *n*-decane (see Figure 4a) increases from zero in the water layer to a bulk value in the oil droplet. Small oscillations are seen inside the droplet before reaching the bulk value.

In Figure 5, the liquid layer between the droplet and the substrate is examined at 3.4 wt % NaCl. The reduced density profiles of ions, water and *n*-decane as a function of the perpendicular distance to the substrate are plotted in Figure 5a. The ion density profiles are normalized to a bulk number density of 0.58 mol/L. The reduced density profile of Na^+ has a sharp peak at $z \approx 0.2$ nm and a small peak at $z \approx 0.42$ nm. The Cl^- reduced density profile shows a peak at $z \approx 0.4$ nm and decreases to zero toward the oil droplet. The surface charge density of muscovite mica is -2.14 e/nm^2. The substrate neutrality is established by the K^+ ions at the outermost layer (2.14 K^+ ions/nm^2) which stay nearly static at their initial position; only about 20 ions out of 756 are released to the solution at $\rho_s = 3.4$ NaCl wt % whereas no ions are released at 0 NaCl wt %. The negative mica surface can adsorb more cations (Na^+) than the necessary number to compensate its bare charge; about 220 Na^+ ions are adsorbed on the whole substrate. This effect is referred as overcharging and is produced by a combination of high substrate charge density, ion−ion, and ion−water many-body correlations.[60−64]

The integral of the Na^+ sharp peak gives 0.37 ions/nm^2 in the confined region implying the substrate is overcharged by 17.3%. Overcharging implies that the number of adsorbed ions exceeds the necessary number to neutralize the surface charge; Cl^- ions in the upper diffuse layer re-establish the overall electroneutrality of the liquid layer. In the bulk solution Na^+ and Cl^- are shielded by 5.4 and 7.3 ions, respectively (see Figure S11, parts a and b). Ions are unlikely found near the *n*-decane-water interface. Na^+ ions adsorbed to the substrate have between 2 to 3 water molecules in their hydration layer (see Figures S11c) at the upper side whereas Cl^- ions in the diffuse layer are fully hydrated.[65,66] Overcharging contributes to higher water adsorption in the liquid layer. The water layer is thicker at 3.4 wt % NaCl (Figure 5a) than at 0 wt % NaCl (Figure 4a); the half density value at 3.4 wt % NaCl is at $z \approx 1.1$ nm whereas at 0 wt % NaCl it is at $z \approx 0.75$ nm. The sharp peak of water oxygen reduced density profile at $z \approx 0.26$ nm, a hump at $z \approx 0.20$ nm, and a secondary peak at $z \approx 0.5$ nm are at about the same position at 0 and at 3.4 wt % NaCl. The reduced density profile of *n*-decane in Figure 5a is shifted upward compared to the profile in in Figure 4a as a consequence of the thicker water layer at higher NaCl concentration. The reduced density profile of *n*-decane monotonically increases from zero in the water layer to a bulk value inside the oil droplet.

The sharp peak of the water density profiles decreases by increasing the salt concentration; it is about 2.2, and 1.6 times the water bulk density at 1.1 and 7.7 NaCl wt %, respectively (see Figures S6 and S7). The height of the secondary peak decreases by increasing the salt concentration. The number of adsorbed Na^+ ions increases by increasing the salt concentration. We will come back to this point toward the end of the paper. Na^+ ions displace water molecules from the first layer on the substrate which is related to the decrease of the adsorbed water molecules as the salt concentration increases.

The snapshot in Figure 5b shows ionic layers adsorbed to the substrate surface. The Na^+ ions are adsorbed on the oxygen outermost layer in the proximity of the K^+ rows. The Cl^- layer is formed on top of the Na^+ and K^+ ions and the diffuse region is also observed. The rotated view in Figure 5c shows the position of the adsorbed ions in a 3D perspective. The unaltered rows of K^+ can be observed. As pointed out earlier the K^+ ions are not restricted; they are left free to move but the strong electrostatic interactions keep them at their positions.

The liquid−solid interface outside the droplet is examined in Figure 6. The density profiles as a function of z are computed within $0 \leq y \leq 5.5$ and 13.5 nm $\leq y \leq$ 18.9 nm. The reduced density profiles of ions and water as a function of the perpendicular distance to the substrate are plotted in Figure 6a. A snapshot of the liquid−solid interface from a section of the simulation box away from the droplet is presented in Figures 6b. The density profile of water shows a small hump at $z \approx 0.20$ nm, a main sharp peak at $z \approx 0.26$ nm and smaller peaks at $z \approx$ 0.5, 0.68, and 0.91 nm (see Figure 6a). The locations of the peaks are characteristic of the water-mica interface and are similar to salt concentrations from 0 to 7.7 wt % NaCl (see Supporting Information). The Na^+ reduced concentration profile shows a sharp peak at the closest approach distance between the ions and the substrate at $z \approx 0.19$ nm, a secondary maximum at $z \approx 0.6$ nm, and reaches the bulk density at around $z \approx 1.2$ nm. The Cl^- reduced density profile shows a peak at $z \approx 0.4$ nm from where it decreases to the bulk value. Electroneutrality is locally broken by the uneven distribution of Na^+ and Cl^- ions at the liquid−solid interface; the overall

DOI: 10.1021/acs.jpcc.6b01521
J. Phys. Chem. C 2016, 120, 11910−11917

electroneutrality is maintained. Integration of the main peak of the Na^+ reduced concentration profile gives surface overcharging by 31.3% (0.67 ions/nm^2); overcharging is higher in the region outside the droplet than in the water layer under the droplet (17.3% at 3.4 wt % NaCl) and increases with salt concentration. Figure 6c shows the reduced density profiles from substrate pre-equilibration (without the droplet). The profiles are qualitatively similar to the profiles in the presence of the droplet (see Supporting Information).

Away from the droplet the main peak height of the water density profiles decreases by increasing the salt concentration; it is about 2.2 and 1.5 at 1.1 and 7.7 NaCl wt %, respectively (see Figures S9 and S10). The number of adsorbed Na^+ ions on the substrate surface increases with the salt concentration; the peak height, however, is about the same because it is a reduced value (see Figures S9 and S10). Figure 7 shows the Na^+ adsorption in the regions under the droplet and away from the droplet. A systematic increase of the ionic adsorption (overcharging) is observed in the regions below and outside the droplet as the salt concentration increases in the bulk; the adsorption is higher away from the droplet than under the droplet. The correlation between the adsorbed ions and the water layer thickness increase as a function of salt concentration is suggested from this analysis (see Figures 3d and 7); higher salt concentration in the bulk induces higher ionic adsorption on the substrate which produces a thicker water layer due to the ionic hydration. As we mentioned above, Cl^- ions form a layer next to Na^+ ions to establish electroneutrality. The ionic and water profiles computed away from the droplet and from the simulations without the oil droplet (pre-equilibration) are qualitatively similar (see Figures S9 and S10) and significant variations of composition are only observed below 1 nm from the substrate.

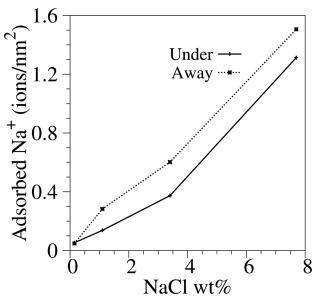

Figure 7. Na^+ adsorption in the region under the droplet (solid line) and away from the droplet (dashed line).

■ CONCLUSIONS

We have computed the liquid−liquid-solid contact angle in the model oil−water−mineral substrate as a function of salt concentration using molecular dynamics simulations; the model oil is *n*-decane and muscovite mica is the solid substrate. In our simulations the contact angle decreases monotonically to a low value as a function of the salt concentration. Our contact angle results are in line with experimental measurements. Higher salt concentration implies a thicker water layer and a decrease of the contact angle in the aqueous phase; at higher salt concentration the substrate becomes less oil-wet. Na^+ and Cl^- ions in the liquid layer are unequally distributed; Na^+ ions adsorb next to the K^+ outermost layer of mica whereas Cl^- ions are at the central region of the liquid layer. A thicker water layer is promoted by increasing salt concentration because ions are highly hydrated; only the ions adsorbed on the substrate are partially dehydrated. Na^+ ion adsorption produces overcharging of the substrate surface; ionic adsorption is higher away from the droplet than in the water layer under the droplet.

■ ASSOCIATED CONTENT

Supporting Information

The Supporting Information is available free of charge on the ACS Publications website at DOI: 10.1021/acs.jpcc.6b01521.

Simulation setups, graphical representation of steps in the setup creation, droplet shapes, thin liquid layer, solid−liquid interface, and ion hydration layer (PDF)

■ AUTHOR INFORMATION

Corresponding Author

*(A.F.) E-mail: abbas.firoozabadi@yale.edu. Telephone: +1 (650)326-9172. Fax: +1 (650) 472-9285.

Notes

The authors declare no competing financial interest.

■ ACKNOWLEDGMENTS

We thank Chevron Corporation and the member companies of the Reservoir Engineering Research Institute (RERI) for their financial support of this work. We thank Dr. Nariman Fathi Najafabadi of Chevron Corporation for his interest and discussions.

■ REFERENCES

(1) Israelachvilli, J. N. *Intermolecular and Surface Forces*, 3rd ed.; Academic Press: London, 1992.

(2) de Gennes, P. G. Wetting: Statics and Dynamics. *Rev. Mod. Phys.* **1985**, *57*, 827−863.

(3) Morrow, N. R. Wettability and Its Effect on Oil Recovery. *JPT, J. Pet. Technol.* **1990**, *42*, 1476−1484.

(4) Anderson, W. Wettability Literature Survey- Part 1: Rock/Oil/Brine Interactions and the Effects of Core Handling on Wettability. *JPT, J. Pet. Technol.* **1986**, *38*, 1125−1144.

(5) Yuan, J.; Liu, X.; Akbulut, O.; Hu, J.; Suib, S.; Kong, J.; Stellacci, F. Superwetting Nanowire Membranes for Selective Absorption. *Nat. Nanotechnol.* **2008**, *3*, 332−336.

(6) Lahann, J. Environmental Nanotechnology: Nanomaterials Clean Up. *Nat. Nanotechnol.* **2008**, *3*, 320−321.

(7) Lahann, J.; Mitragotri, S.; Tran, T. N.; Kaido, H.; Sundaram, J.; Choi, I. S.; Hoffer, S.; Somorjai, G. A.; Langer, R. A Reversibly Switching Surface. *Science* **2003**, *299*, 371−374.

(8) Firoozabadi, A. *Thermodynamics and Applications in Hydrocarbons Energy Production*; Mc Grow Hill: 2015.

(9) Tang, G. Q.; Morrow, N. R. Influence of Brine Composition and Fines Migration on Crude Oil/Brine/Rock Interactions and Oil Recovery. *J. Pet. Sci. Eng.* **1999**, *24*, 99−111.

(10) Shalabi, E. W. A.; Sepehrnoori, K.; Delshad, M. Mechanisms Behind Low Salinity Water Injection in Carbonate Reservoirs. *Fuel* **2014**, *121*, 11−19.

(11) Mugele, F.; Bera, B.; Cavalli, A.; Siretanu, I.; Maestro, A.; Duits, M.; Cohen-Stuart, M.; van den Ende, D.; Stocker, I.; Collins, I. Ion Adsorption-Induced Wetting Transition in Oil-Water-Mineral Systems. *Sci. Rep.* **2015**, *5*, 10519.

(12) Aslan, S.; Fathi Najafabadi, N.; Firoozabadi, A. Non-monotonicity of the Contact Angle from NaCl and MgCl2 Concentrations in Two Petroleum Fluids on Atomistically Smooth Surfaces. *Energy Fuels* **2016**, *30*, 2858.

(13) Myint, P. C.; Firoozabadi, A. Thin Liquid Films in Improved Oil Recovery from Low-Salinity Brine. *Curr. Opin. Colloid Interface Sci.* **2015**, *20*, 105−114.

DOI: 10.1021/acs.jpcc.6b01521
J. Phys. Chem. C 2016, 120, 11910−11917

(14) Lee, S. Y.; Webb, K. J.; Collins, I.; Lager, A.; Clarke, S.; O'Sullivan, M.; Routh, A.; Wang, X. Low Salinity Oil Recovery: Increasing Understanding of the Underlying Mechanisms. Presented at IOR 2011—16th European Symposium on Improved Oil Recovery.
(15) Sikkenk, J. H.; Indekeu, J. O.; van Leeuwen, J. M. J.; Vossnack, E. O. Molecular-Dynamics Simulation of Wetting and Drying at Solid-Fluid Interfaces. *Phys. Rev. Lett.* **1987**, *59*, 98−101.
(16) Ingebrigtsen, T.; Toxvaerd, S. Contact Angles of Lennard-Jones Liquids and Droplets on Planar Surfaces. *J. Phys. Chem. C* **2007**, *111*, 8518−8523.
(17) Shi, B.; Dhir, V. K. Molecular Dynamics Simulation of the Contact Angle of Liquids on Solid Surfaces. *J. Chem. Phys.* **2009**, *130*, 034705.
(18) Weijs, J. H.; Marchand, A.; Andreotti, B.; Lohse, D.; Snoeijer, J. H. Origin of Line Tension for a Lennard-Jones Nanodroplet. *Phys. Fluids* **2011**, *23*, 022001.
(19) Becker, S.; Urbassek, H. M.; Horsch, M.; Hasse, H. Contact Angle of Sessile Drops in Lennard-Jones Systems. *Langmuir* **2014**, *30*, 13606−13614.
(20) Savoy, E. S.; Escobedo, F. A. Molecular Simulations of Wetting of a Rough Surface by an Oily Fluid: Effect of Topology, Chemistry, and Droplet Size on Wetting Transition Rates. *Langmuir* **2012**, *28*, 3412−3419.
(21) Wang, F.-C.; Zhao, Y.-P. Contact Angle Hysteresis at the Nanoscale: A Molecular Dynamics Simulation Study. *Colloid Polym. Sci.* **2013**, *291*, 307−315.
(22) Lundgren, M.; Allan, N. L.; Cosgrove, T.; George, N. Wetting of Water and Water/Ethanol Droplets on a Non-Polar Surface: A Molecular Dynamics Study. *Langmuir* **2002**, *18*, 10462−10466.
(23) Metya, A. K.; Khan, S.; Singh, J. K. Wetting Transition of the Ethanol−Water Droplet on Smooth and Textured Surfaces. *J. Phys. Chem. C* **2014**, *118*, 4113−4121.
(24) Isele-Holder, R. E.; Berkels, B.; Ismail, A. E. Smoothing of contact lines in spreading droplets by trisiloxane surfactants and its relevance for superspreading. *Soft Matter* **2015**, *11*, 4527−4539.
(25) Shen, Y.; Couzis, A.; Koplik, J.; Maldarelli, C.; Tomassone, M. S. Molecular Dynamics Study of the Influence of Surfactant Structure on Surfactant-Facilitated Spreading of Droplets on Solid Surfaces. *Langmuir* **2005**, *21*, 12160−12170.
(26) Halverson, J. D.; Maldarelli, C.; Couzis, A.; Koplik, J. Wetting of Hydrophobic Substrates by Nanodroplets of Aqueous Trisiloxane and Alkyl Polyethoxylate Surfactant Solutions. *Chem. Eng. Sci.* **2009**, *64*, 4657−4667.
(27) Sergi, D.; Scocchi, G.; Ortona, A. Molecular Dynamics Simulations of the Contact Angle Between Water Droplets and Graphite Surfaces. *Fluid Phase Equilib.* **2012**, *332*, 173−177.
(28) Shih, C.-J.; Wang, Q. H.; Lin, S.; Park, K.-C.; Jin, Z.; Strano, M. S.; Blankschtein, D. Breakdown in the Wetting Transparency of Graphene. *Phys. Rev. Lett.* **2012**, *109*, 176101.
(29) Werder, T.; Walther, J. H.; Jaffe, R. L.; Halicioglu, T.; Noca, F.; Koumoutsakos, P. Molecular Dynamics Simulation of Contact Angles of Water Droplets in Carbon Nanotubes. *Nano Lett.* **2001**, *1*, 697−702.
(30) Rafiee, J.; Mi, X.; Gullapalli, H.; Thomas, A. V.; Yavari, F.; Shi, Y.; Ajayan, P. M.; Koratkar, N. A. Wetting Transparency of Graphene. *Nat. Mater.* **2012**, *11*, 217−222.
(31) Shih, C.-J.; Strano, M.-S.; Blankschtein, D. Wetting Translucency of Graphene. *Nat. Mater.* **2013**, *12*, 866.
(32) Scocchi, G.; Sergi, D.; D'Angelo, C.; Ortona, A. Wetting and Contact-Line Effects for Spherical and Cylindrical Droplets on Graphene Layers: A Comparative Molecular-Dynamics Investigation. *Phys. Rev. E* **2011**, *84*, 061602.
(33) Taherian, F.; Marcon, V.; van der Vegt, N. F. A.; Leroy, F. What is the Contact Angle of Water on Graphene? *Langmuir* **2013**, *29*, 1457−1465.
(34) Wu, C. D.; Kuo, L. M.; Lin, S. J.; Fang, T. H.; Hsieh, S. F. Effects of Temperature, Size of Water Droplets, and Surface Roughness on Nanowetting Properties Investigated Using Molecular Dynamics Simulation. *Comput. Mater. Sci.* **2012**, *53*, 25−30.
(35) Solc, R.; Gerzabek, M. H.; Lischka, H.; Tunega, D. Wettability of Kaolinite Surfaces: Molecular Dynamic Study. *Geoderma* **2011**, *169*, 47−54.
(36) Giovambattista, N.; Debenedetti, P. G.; Rossky, P. J. Effect of Surface Polarity on Water Contact Angle and Interfacial Hydration Structure. *J. Phys. Chem. B* **2007**, *111*, 9581−9587.
(37) Chai, J.; Liu, S.; Yang, X. Molecular Dynamics Simulation of Wetting on Modified Amorphous Silica Surface. *Appl. Surf. Sci.* **2009**, *255*, 9078−9084.
(38) Ohler, B.; Langel, W. Molecular Dynamics Simulations on the Interface between Titanium Dioxide and Water Droplets: A New Model for the Contact Angle. *J. Phys. Chem. C* **2009**, *113*, 10189−10197.
(39) Rotenberg, B.; Patel, A. J.; Chandler, D. Molecular Explanation for Why Talc Surfaces Can Be Both Hydrophilic and Hydrophobic. *J. Am. Chem. Soc.* **2011**, *133*, 20521−20527.
(40) Fan, C. F.; Cağin, T. Wetting of Crystalline Polymer Surfaces: A Molecular Dynamics Simulation. *J. Chem. Phys.* **1995**, *103*, 9053−9061.
(41) Hirvi, J. T.; Pakkanen, T. A. Molecular Dynamics Simulations of Water Droplets on Polymer Surfaces. *J. Chem. Phys.* **2006**, *125*, 144712.
(42) Factorovich, M. H.; Molinero, V.; Scherlis, D. A. Hydrogen-Bond Heterogeneity Boosts Hydrophobicity of Solid Interfaces. *J. Am. Chem. Soc.* **2015**, *137*, 10618−10623.
(43) Koishi, T.; Yasuoka, K.; Fujikawa, S.; Zeng, X. C. Measurement of Contact-Angle Hysteresis for Droplets on Nanopillared Surface and in the Cassie and Wenzel States: A Molecular Dynamics Simulation Study. *ACS Nano* **2011**, *5*, 6834−6842.
(44) Iglauer, S.; Mathew, M. S.; Bresme, F. Molecular Dynamics Computations of Brine-CO2 Interfacial Tensions and Brine-CO2-Quartz Contact Angles and Their Effects on Structural and Residual Trapping Mechanisms in Carbon Geo-Sequestration. *J. Colloid Interface Sci.* **2012**, *386*, 405−414.
(45) Tenney, C. M.; Cygan, R. T. Molecular Simulation of Carbon Dioxide, Brine, and Clay Mineral Interactions and Determination of Contact Angles. *Environ. Sci. Technol.* **2014**, *48*, 2035−2042.
(46) Seveno, D.; Blake, T. D.; Goossens, S.; De Coninck, J. Predicting the Wetting Dynamics of a Two-Liquid System. *Langmuir* **2011**, *27*, 14958−14967.
(47) Kumar, V.; Errington, J. R. Understanding Wetting of Immiscible Liquids Near a Solid Surface Using Molecular Simulation. *J. Chem. Phys.* **2013**, *139*, 064110.
(48) Martin, M. G.; Siepmann, J. I. Transferable Potentials for Phase Equilibria. 1. United-Atom Description of n-Alkanes. *J. Phys. Chem. B* **1998**, *102*, 2569−2577.
(49) Berendsen, H. J. C.; Postma, J. P. M.; van Gunsteren, W. F.; Hermans, J. In *Intermolecular Forces*; Pullman, B., Ed.; Reidel: Dordrecht, The Netherlands, 1981; Chapter: Simple Point Charge Water.
(50) Jørgensen, W. L. In *The Encyclopedia of Computational Chemistry*; Schleyer, P. v. R., Ed.; John Wiley & Sons: Dordrecht, The Netherlands, 1998; Vol. 3; Chapter: OPLS Force Fields.
(51) Heinz, H.; Koerner, H.; Anderson, K. L.; Vaia, R. A.; Farmer, B. L. Force Field for Mica-Type Silicates and Dynamics of Octadecylammonium Chains Grafted to Montmorillonite. *Chem. Mater.* **2005**, *17*, 5658−5669.
(52) Guven, N. The Crystal Structures of 2M1 Phengite and 2M1Muscovite. *Z. Kristallogr. - Cryst. Mater.* **1971**, *134*, 196−212.
(53) Abraham, F. F.; Singh, Y. The Structure of a Hard-Sphere Fluid in Contact with a Soft Repulsive Wall. *J. Chem. Phys.* **1977**, *67*, 2384−2385.
(54) Yeh, I.-C.; Berkowitz, M. L. Ewald Summation for Systems with Slab Geometry. *J. Chem. Phys.* **1999**, *111*, 3155−3162.
(55) Nosé, S. A. Unified Formulation of the Constant Temperature Molecular-Dynamics Methods. *J. Chem. Phys.* **1984**, *81*, 511−519.
(56) Hoover, W. G. Canonical Dynamics: Equilibrium Phase-Space Distributions. *Phys. Rev. A: At., Mol., Opt. Phys.* **1985**, *31*, 1695−1697.

DOI: 10.1021/acs.jpcc.6b01521
J. Phys. Chem. C 2016, 120, 11910−11917

(57) Van Der Spoel, D. V. D.; Lindahl, E.; Hess, B.; Groenhof, G.; Mark, A. E.; Berendsen, H. J. C. GROMACS: Fast, Flexible, and Free. *J. Comput. Chem.* **2005**, *26*, 1701−1718.
(58) Hess, B.; Kutzner, C.; van der Spoel, D.; Lindahl, E. GROMACS 4: Algorithms for Highly Efficient, Load-Balanced, and Scalable Molecular Simulation. *J. Chem. Theory Comput.* **2008**, *4*, 435−447.
(59) Schultz, J.; Tsutsumi, K.; Donnet, J.-B. Surface Properties of High-Energy Solids. *J. Colloid Interface Sci.* **1977**, *59*, 272−276.
(60) Attard, P.; Prigogine, I.; Rice, S. A. Electrolytes and the Electric Double Layer. *Adv. Chem. Phys.* **1996**, *92*, 1−159.
(61) Messina, R.; González-Tovar, E.; Lozada-Cassou, M.; Holm, C. Overcharging: The Crucial Role of Excluded Volume. *EPL (Europhysics Letters)* **2002**, *60*, 383.
(62) Jiménez-Ángeles, F.; Lozada-Cassou, M. On the Regimes of Charge Reversal. *J. Chem. Phys.* **2008**, *128*, 174701.
(63) Jiménez-Ángeles, F. Effects of Mixed Discrete Surface Charges on the Electrical Double Layer. *Phys. Rev. E* **2012**, *86*, 021601.
(64) Lyklema, J. Overcharging, Charge reversal: Chemistry or Physics? *Colloids Surf., A* **2006**, *291*, 3−12.
(65) Ricci, M.; Spijker, P.; Stellacci, F.; Molinari, J.-F.; Voïtchovsky, K. Direct Visualization of Single Ions in the Stern Layer of Calcite. *Langmuir* **2013**, *29*, 2207−2216.
(66) Ricci, M.; Spijker, P.; Voïtchovsky, K. Water-Induced Correlation Between Single Ions Imaged at the Solid-Liquid Interface. *Nat. Commun.* **2014**, *5*, 4400.

DOI: 10.1021/acs.jpcc.6b01521
J. Phys. Chem. C 2016, 120, 11910−11917